Computational Condensed Matter 46 (2026) e01181

Contents lists available at ScienceDirect

Computational Condensed Matter

journal homepage: www.elsevier.com/locate/cocom

Full length article

Unraveling the structural, optoelectronic, and mechanical properties of calcium sulfate

Marcelo F.S. Santos [a], Carlos H.P. Silva [a], Ivana M.G.A. Cavalcanti [a], Danilo O. Junot [b] Anderson M.B. Silva [c], Marcos V.S. Rezende [a], Érico R.P. Novais [d], Linda V.E. Caldas [c] Andréa L.F. Novais [e,*], Divanizia N. Souza [a]

[a] Departamento de Física, Universidade Federal de Sergipe, Av. Marechal Rondon, S/N, 49.100-000, São Cristovão, SE, Brazil
[b] Instituto de Física Armando Dias Tavares, Universidade do Estado do Rio de Janeiro, Rio de Janeiro, RJ, Brazil
[c] Instituto de Pesquisas Energéticas e Nucleares, Comissão Nacional de Energia Nuclear, IPEN/CNEN-SP, Av. Prof. Lineu Prestes, 2242, 05508-000, São Paulo, SP, Brazil
[d] Faculdade de Física, Universidade Federal do Sul e Sudeste do Pará, Marabá, PA, Brazil
[e] Faculdade de Engeharia Mecânica, Universidade Federal do Sul e Sudeste do Pará, Marabá, PA, Brazil

ARTICLE INFO

Keywords:
DFT
Theoretical study
Physical properties

ABSTRACT

Although calcium sulfate ($CaSO_4$) has been the subject of experimental research for many decades, several fundamental aspects of its physical behavior remain unresolved. In this work, we present a comprehensive theoretical investigation aimed at unraveling its structural, optoelectronic, and mechanical properties using first-principles calculations based on density functional theory. Structural optimization was performed using the density approximation, LDA, PBE, and PBEsol exchange–correlation functionals, which are suitable for accurately describing the structural, electronic, optical, and mechanical interactions within the system. To enhance the description of the electronic structure, we also employed the shielded HSE06 hybrid exchange–correlation functional, which resulted in a bandgap of E_g = 7.271 eV, in contrast to the value of E_g = 6.044 eV obtained with the semilocal PBEsol functional. The compound exhibited polarization-dependent optical absorption in the ultraviolet range, remaining practically isotropic. The estimated cohesive energy and phonon dispersion confirmed strong interatomic binding and high phonon frequencies. Furthermore, the values obtained for the elastic constants demonstrated that $CaSO_4$ possesses high structural stability, suggesting its potential use in optoelectronic devices and as an insulating material in microelectronic systems. Overall, our findings provide a detailed understanding of the physical properties of $CaSO_4$, consistent with the goal of unraveling its fundamental behavior.

1. Introduction

$CaSO_4$ is a highly versatile compound with a wide range of potential applications, primarily due to its ability to exist in various hydration states. In its hemihydrate form ($CaSO_4 \cdot \frac{1}{2}H_2O$), commonly known as plaster of Paris, it can be obtained in two distinct polymorphs, α and β. The α-form exhibits a more fibrous, porous, and irregular structure, which promotes agglomeration, whereas the β-form shows cleavage along well-defined planes, forming crystallites with needle-like or prismatic morphology [1].

These different microstructural forms strongly influence the final properties of the material after dehydration, particularly in terms of its hardness and mechanical strength [1,2]. These characteristics are highly desirable for a diverse range of applications including civil construction, cements, drywall coatings, ceramics, artistic plaster, dentistry, dental casts, and orthopedics (bone grafts, immobilization, and bone regeneration) [3–5]. In agriculture, $CaSO_4$ functions as a fertilizer due to its physical and chemical properties in its dihydrate form ($CaSO_4 \cdot 2H_2O$); known as gypsum, it serves as a soil conditioner, helping to slow down soil degradation and to mitigate the harmful effects of heavy metals [6–8].

In medical physics, and specifically in the field of ionizing radiation dosimetry, dehydrated $CaSO_4$ (anhydrite), which is obtained after calcination, has emerged as an effective matrix when doped with rare earth and transition metals [9–12]. This material exhibits high sensitivity and excellent dose–response linearity when used as a dosimeter with thermoluminescence and optically stimulated luminescence techniques. Moreover, in some cases, it demonstrates low fading levels [13–18].

* Corresponding author.
E-mail address: andreanovais@unifesspa.edu.br (A.L.F. Novais).

https://doi.org/10.1016/j.cocom.2025.e01181
Received 18 August 2025; Received in revised form 24 November 2025; Accepted 25 November 2025
Available online 25 November 2025

The applications and performance of $CaSO_4$ are directly related to the synthesis pathways employed in its production. Common routes include slow evaporation synthesis (which involves mixing sulfuric acid with calcium carbonate and heating until acid evaporation) [19,20]; solid-state diffusion reactions (involving the mixing of $CaSO_4{\cdot}2H_2O$ with dopants followed by hydration) [21]; sol–gel processes (involving the mixing of calcium chloride, ethanol, ammonium sulfate, and dopants under stirring) [22]; co-precipitation (involving the mixing of calcium acetate, ethanol, ammonium sulfate, and dopants under stirring) [23]; and hydrothermal methods involving thermal treatment in autoclaves [24].

At the atomic scale, the role of water molecules in amorphous $CaSO_4$ is fundamental, as they influence ion transport, local coordination, and structural evolution towards crystalline phases [25]. Vacancy defects in the crystal lattice, such as those associated with Ca, SO_4, and H_2O, have been found to strongly affect the adsorption and incorporation of impurity atoms, and particularly toxic metals such as cadmium, by modulating local electronic structure and bonding [26]. According to Junot (2024) [18], the incorporation of rare-earth (RE^{3+}) ions into Ca sites may lead to the formation of Ca vacancies as a charge-compensation mechanism. When two RE^{3+} ions replace two Ca^{2+} ions, the resulting charge imbalance of +2 is counterbalanced by the creation of a single Ca cation vacancy, thereby preserving the overall electroneutrality and stabilizing the lattice. These defects govern the material's capacity for environmental remediation, and impact its surface chemistry and stability.

A combination of dispersion-corrected density functional theory (DFT) and first-principles molecular dynamics allows for a detailed investigation of defect–impurity interactions at the atomic level, and predictions of defect stability, impurity formation energies, adsorption mechanisms, and dynamic behaviors over timescales of femtoseconds to nanoseconds [26]. This computational approach provides mechanistic insights that are inaccessible via experiments alone, and enables the rational design of materials with tailored properties. In addition, DFT studies reveal that doping $CaSO_4$ with alkali metal sulfates such as Na_2SO_4 enhances its performance for applications such as calcium looping for thermochemical energy storage by modifying the surface energies and preventing sintering [27]. These findings highlight the fundamental role of first-principles simulations in guiding material optimization.

Given the significant influence of the synthesis method, microstructure, water content, and vacancy defects on the physical properties and applications of calcium sulfate, there is an imperative need to deepen the current understanding of its structural, electronic, optical, and mechanical behaviors at the atomic scale. First-principles calculations based on DFT offer an essential tool for this endeavor [28].

While most studies on calcium sulfate have focused on macroscopic behavior or hydrated phases, its atomic-scale properties remain largely unexplored. Here, we present, for the first time in an integrated manner, an ab initio investigation of anhydrous orthorhombic $CaSO_4$, examining structural, electronic, optical, and mechanical properties. Using comprehensive DFT calculations, we elucidate key physical properties, including lattice parameters, electronic structure, optical response, and mechanical behavior. These atomic-scale insights aim to support the development and optimization of $CaSO_4$ for multifunctional applications, spanning environmental remediation, biomedical engineering, and energy technologies.

2. Computational details

All calculations in this work were performed using the plane–wave self–consistent field method, as implemented in the Cambridge Serial Total Energy Package (CASTEP) code [29], which is based on DFT techniques [30]. The orthorhombic unit cell of $CaSO_4$, which contains 12 atoms in its primitive unit, was obtained from the Materials Project repository [31] and used as the starting structure for first-principles calculations. To enable a systematic evaluation of the role of the exchange–correlation functional, four different schemes were employed: the local density approximation (LDA) [32] using the Perdew–Zunger parameterization [33]; the generalized gradient approximation (GGA) in the form of the Perdew–Burke–Ernzerhof (PBE) functional [34]; revised PBEsol functional [35], which was specifically designed for improved structural and mechanical predictions in solids; and the Heyd–Scuseria–Ernzerhof hybrid exchange–correlation functional [36] with optimized screening parameters (HSE06) [37], which is recommended for bandgap calculations in the CASTEP code [29].

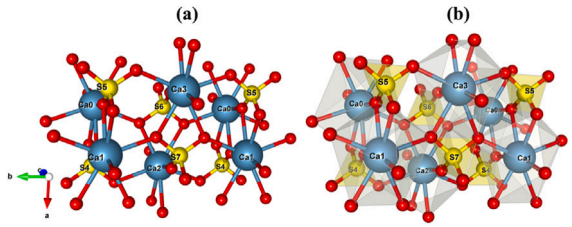

Fig. 1. Crystal structure of orthorhombic $CaSO_4$ obtained using VESTA: (a) atomic representation and (b) polyhedral representation.

Pseudopotentials were generated on-the-fly (OTFG) during the calculations, employing the following electronic states: Ca ($3s^2\ 3p^6\ 4s^2$), S ($3s^2\ 3p^4$), and O ($2s^2\ 2p^4$). A plane-wave cutoff energy of 620.00 eV was employed, and the Brillouin zone was sampled using a Monkhorst–Pack k-point mesh of $6 \times 5 \times 5$ [38]. This configuration was used for the geometric optimization of the unit cell within the non-hybrid exchange–correlation functionals (LDA, PBE, and PBEsol). For the calculations involving the hybrid functional (HSE06), the geometric optimization of the primitive cell and the subsequent electronic band structure calculations were performed using a cutoff energy of 625.90 eV, with the Brillouin zone sampled by a Monkhorst–Pack k-point mesh of $3 \times 3 \times 2$ [38]. Electronic self-consistency and structural relaxation were both performed using the Broyden–Fletcher–Goldfarb–Shanno (BFGS) algorithm [39]. The convergence thresholds were set as follows: a total energy of below $\times\ 10^{-6}$ eV/atom, a maximum force of below 0.01 eV/Å, a residual stress of less than 0.02 GPa, and a maximum ionic displacement of 0.0005 Å. Phonon dispersion relations were calculated within the harmonic approximation as implemented in CASTEP [29], and elastic constants were computed after full structural relaxation to evaluate the mechanical stability and anisotropy.

The Elastic Analysis Tool for Elasticity (ELATE) program [40] was employed to analyze and visualize the two and three-dimensional elastic properties, including the Young's modulus (Y), linear compressibility (β), shear modulus (G), and Poisson's ratio (ν), providing both qualitative and quantitative insights into the anisotropic elastic response of the material.

3. Results and discussion

3.1. Structural properties

Fig. 1 shows that orthorhombic $CaSO_4$ crystallizes in the *Cmcm* (No. 63) space group [31]. The Ca, S, and O atoms occupy specific Wyckoff positions within the conventional unit cell: 4c (0.350952, 0, 3/4) for Ca, 4c (0.847663, 0, 3/4) for S, and 8f (0.294832, 0, 0.08153) and 8 g (0.488467, 0.670058, 3/4) for O. The atomic (Fig. 1a) and polyhedral (Fig. 1b) representations of the orthorhombic $CaSO_4$ unit cell show 6 Ca atoms (blue spheres), 6 S atoms (light-yellow spheres), and 42 O atoms (red spheres), giving a total of 54 atoms in the conventional unit cell.

Table 1 presents the results of the structural optimization obtained using the four different functionals (LDA, PBE, PBEsol, and HSE06) for the primitive $CaSO_4$ cell. The table presents the optimized lattice constants, unit cell volumes (V), and total electronic energies (E_T)

Table 1
Structural and energetic parameters of primitive $CaSO_4$ cell obtained using different functionals (relative percentage deviations calculated with respect to MP-4406 reference data).

Parameter	MP-4406	LDA	Δ%	PBE	Δ%	PBEsol	Δ%	HSE06	Δ%
$a = b$ (Å)	4.67	4.58	1.93	4.75	1.71	4.67	0.00	4.95	6.00
c (Å)	7.01	6.89	1.71	7.10	1.28	7.00	0.14	7.22	3.00
V (Å^3)	158.52	144.20	9.03	159.24	0.45	151.86	4.20	176.03	11.05
E_T (eV)	–	-6.141×10^3	–	-6.141×10^3	–	-6.131×10^3	–	-6.110×10^3	–

Table 2
Bond lengths (Å) in primitive $CaSO_4$ cell obtained with different functionals (deviations are relative to MP-4406 data).

Parameter	MP-4406	LDA	Δ%	PBE	Δ%	PBEsol	Δ%	HSE06	Δ%
Ca–O_1	2.58	2.48	3.88	2.59	0.39	2.53	1.94	2.51	2.71
Ca–O_2	2.37	2.29	3.38	2.37	0.00	2.33	1.69	2.46	3.80
S–O_1	1.48	1.47	0.68	1.49	0.95	1.48	0.00	1.45	2.03
S–O_2	1.49	1.47	1.34	1.49	0.00	1.48	0.67	1.47	1.34

computed under fixed-volume conditions (0 K and approximately zero external pressure), together with the relative deviations (Δ%) with respect to the MP-4406 reference data. This set of structural and energetic parameters provides a rigorous quantitative benchmark for evaluating the accuracy, internal consistency, and thermodynamic stability of the investigated theoretical models.

From Table 1, it can be seen that the calculations performed with the PBEsol functional provided the best overall agreement with the reference structure, especially in regard to the lattice constants a and b = 4.67 Å which are reproduced with zero uncertainty. Although total energy comparisons are reported, they should be interpreted with caution, since absolute values may vary across functionals, for example of the formation or cohesion energy. As expected, LDA consistently underestimated the lattice dimensions and volume due to its well-known overbinding tendency. The PBE functional yielded the closest volume to MP-4406, making it more suitable for volume-dependent property predictions. And HSE06 yields the largest overestimation of the volume ($\Delta V \approx 11.05\%$) . These structures correspond to the primitive cell of $CaSO_4$, obtained through the automatic transformation performed by the CASTEP code [29] to reduce computational cost, since the orthorhombic unit cell associated with the *Cmcm* (No. 63) space group can be reconstructed by applying the symmetry operations of this optimized structure.

Table 2 presents the Ca–S and S–O bond lengths (in Å) calculated for orthorhombic $CaSO_4$ using four different functionals (LDA, PBE, PBEsol, and HSE06) for orthorhombic $CaSO_4$, together with the relative uncertainties (Δ%) with respect to the MP-4406 reference structure. The results show that PBE provides the best agreement, with minimal or zero uncertainty for several bonds, particularly Ca-O_2 and S–O_2. LDA tends to underestimate the bond lengths, as expected due to its overbinding behavior, while PBEsol generally yields intermediate accuracy. The S–O bonds are more rigidly constrained, with smaller variations across functionals, which indicates their stronger and less functional-dependent character.

The local geometry influences key properties of the $CaSO_4$, such as its rigidity, optical response, vibrational behavior, and structural stability. The presence of asymmetric angle values confirms the absence of perfect local symmetry around Ca, which is common in complex structures or in lower-symmetry phases such as orthorhombic systems.

3.2. Phonon dispersion and cohesive energy

Phonon dispersion describes how the frequency of atomic vibrations varies with the wave vector in a crystal. It provides key information on dynamic stability, thermal conductivity, and modes of vibration, both acoustic and optical. This behavior was experimentally verified by Schweiss et al. [41], who measured the phonon dispersion of anhydrite and successfully modeled it using a rigid-ion approach in which SO_4^{2-}–groups were treated as quasi-rigid units. The agreement found by these authors between experimental and theoretical results validates the harmonic approximation used in this study. Additional evidence presented by Korabel'nikov and Zhuravlev [42] shows that sulfates such as $CaSO_4$ have high elastic stiffness and low thermal conductivity, due to their strong ionic interactions and vibrational stability. These properties make orthorhombic $CaSO_4$ a promising material for dielectric and thermal insulation applications. In summary, the absence of imaginary phonon frequencies and the weak electron–phonon coupling indicate low electrical conductivity and moderate thermal conductivity. These characteristics reinforce the potential of orthorhombic $CaSO_4$ for applications in optoelectronics, dielectric devices, functional ceramics, and sensors [41].

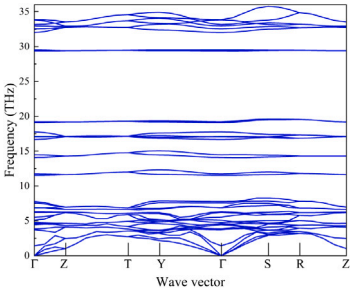

Fig. 2. Phonon dispersion curves for orthorhombic $CaSO_4$ over the frequency range zero to 35.0 THz.

Fig. 2 shows phonon dispersion curves for selected high-symmetry directions (Γ, Z, T, Y, Γ, S, R, Z) in the Brillouin zone, which were calculated using the GGA-PBEsol functional. These curves cover the frequency range from zero to 35.0 THz, and include 36 distinct modes. The absence of imaginary frequencies throughout the Brillouin zone confirms the dynamic stability of the orthorhombic $CaSO_4$ phase. Phonon dispersion extends up to ~35.0 THz (≈1167 cm^{-1}). The maximum frequency of the acoustic branches reaches ~6.0 THz (≈200 cm^{-1}), while the optical modes extend up to ~35.0 THz (≈1167 cm^{-1}). These high-frequency optical phonons are consistent with the wide-bandgap of the material (see Fig. 2) and are typical of those observed for oxide compounds. Clear separation between the acoustic and optical branches is also observed, reinforcing the vibrational stability of the orthorhombic $CaSO_4$.

The cohesive energy per atom is defined as the average energy required to disaggregate each particle, atoms, ions, or molecules, in a system [43,44]. The cohesive energies were computed using the following formula:

$$E_{coh} = \frac{E_{Ca}^{isolated} + E_{S}^{isolated} + E_{O}^{isolated} - E_{CaSO_4}^{tot}}{n + m + l} \quad (1)$$

Table 3
Isolated atomic energies and total energy of the orthorhombic $CaSO_4$ primitive cell.

Element	Energy (eV)
$E_{Ca}^{isolated}$	−1001.1307
$E_{S}^{isolated}$	−298.6408
$E_{O}^{isolated}$	−431.1226
$E_{CaSO_4}^{tot}$	−6131.2162

wher $E_{Ca}^{isolated}$, $E_{S}^{isolated}$, and $E_{O}^{isolated}$ are the total energies of isolated Ca, S, and O atoms, respectively; $E_{CaSO_4}^{tot}$ is the total energy of the relaxed $CaSO_4$ primitive cell; and $n = 2$, $m = 2$, and $l = 8$ represent the numbers of atoms of each element in the primitive cell.

Table 3 shows the energy values calculated for each isolated atom and for the bound structure using GGA-PBEsol. The cohesive energy per atom, estimated based on Equation (1) and Table 3, was approximately E_{coh}= 6.891 eV/atom. This high value for the cohesive energy indicates strong structural stability, suggesting the presence of robust and rigid interatomic bonds. Increased bond stiffness leads to higher phonon frequencies and, consequently, a broader phonon dispersion across the Brillouin zone. Gracia et al. [45] performed a detailed DFT study of $CaSO_4$ under pressure, and confirmed that the orthorhombic anhydrite phase is the most stable under ambient conditions, remaining structurally stable up to 5.0 GPa. This finding supports the structural and thermodynamic stability that can be inferred from the cohesive energy.

3.3. Kohn–Sham electronic band structure, PDOS and TDOS

Figs. 3(a and c), on the left, show the Kohn–Sham band structure along the path (Γ, Z, T, Y, Γ, S, R, Z), and Figs. 3(b and d), on the right, show the total and projected density of states (TDOS/PDOS) of $CaSO_4$, calculated based on the exchange–correlation potential using the PBEsol functional and the hybrid functional HSE06. The PDOS show the contributions of O 2s/2p, S 3s/3p and Ca 3s/3p/3d. The PBEsol functional underestimates the bandgap, E_g = 6.044 eV, which is a well-documented limitation of local/generalized density approximations [35]. The application of the hybrid HSE06 functional [36] corrects this underestimation, increasing the value to E_g = 7.271 eV, thereby demonstrating the known correction for the delocalization error (see Figs. 3(a–d). Both functionals predict an indirect (Y→ Γ) wide-bandgap; HSE06 increases the gap and shifts the Ca 3d-derived conduction bands to higher energies. HSE06 also yielded a considerably wider valence band (VB) (1.80 eV) compared to PBEsol (0.9 eV), suggesting greater dispersion in the valence band. The dominant orbital contributions, O 2p at the valence band maximum (VBM) and Ca 3d at the conduction band minimum (CBM), are typical for alkaline-earth metal oxides. The calculated effective masses (m^*) for HSE06 indicate a hole mass ($m_h^* \approx 2.5\, m_e$) that is larger than the electron mass ($m_e^* \approx 0.9\, m_e$), a pattern similar to that observed in PBEsol [46]. The high hole mass suggests low mobility and a more localized nature of the VBM, which is in good agreement with the greater VB dispersion observed in HSE06 compared to the flatter VB in PBEsol. The discrepancy in E_g and the enhanced dispersion and consequently higher m_h^* calculated by HSE06 underscore the importance of hybrid functionals for the accurate description of the electronic structure of wide-bandgap insulators.

Experimental approaches such as the work developed by Nagabhushana et al. (2010) reported optical bandgap values of 5.0 and 5.35 for $CaSO_4$ in commercial form and pseudomicrorods, respectively [47]. In the work developed by Salikhodzha et al. (2019), the authors address luminescent recombination in $CaSO_4$ crystals and estimate a bandgap value of 5.0 eV [48]. Junot et al. (2019) studied the behavior of $CaSO_4$ crystals doped with Tm and Ag for dosimetry applications. In this article, the authors associate the optical absorption band around 8.2 eV with the host lattice, i.e., the bandgap of $CaSO_4$ [49]. Using a DFT approach, Mandlik et al. (2020) found values between 5.67–5.86 eV for both orthorhombic and hexagonal $CaSO_4$ structures [50]. Accordingly, the estimated bandgaps of E_g = 6.044 eV (PBEsol) and E_g = 7.271 eV (HSE06) are in good agreement with previously reported values.

3.4. Optical properties

Fig. 4 shows the optical absorption coefficient of orthorhombic $CaSO_4$, highlighting regions I, II, III, and IV, which correspond to the absorption maxima along the crystallographic directions (100), (010), (001), (011), and (111). Region I, in the energy range from 5.0 eV (248 nm) to 12.5 eV (100 nm), lies within the ultraviolet (UV) spectrum, more specifically in the UV-C region (100–280 nm) [51]. In this range, a slight shoulder appears around 8.2 eV (151 nm), which can be attributed to the promotion of valence band (VB) electrons to conduction band (CB) states, a process directly related to the band gap of the material, as experimentally reported by Junot et al. (2019) [49]. The absorption increases until reaching a well-defined peak around 10.4 eV (120 nm), which can be assigned to intraband transitions originating from the O–2p orbitals to Ca–3d states. The other regions (II, III, and IV) belong to the extreme ultraviolet (EUV) or soft X-ray spectral range [52]. In these regions, distinct absorption peaks are observed at 13.2 eV (94 nm), 17.6 eV (70.4 nm), and 27 eV (46 nm), which are likely associated with the K, L, and M edge absorptions of the constituent ions, indicating deeper electronic transitions within the atomic levels of the compound.

The spectral regions analyzed are highlighted by colored bands in the Fig. 4. Region I (5.0–12.0 eV), shown in dark blue, corresponds to the domain of low-energy optical transitions. Region II (12.0–15.0 eV) appears in medium blue, indicating a gradual increase in the absorption coefficient associated with the onset of interband transitions. Region III (15.0–22.0 eV) is represented by the light–blue band and covers the interval where more intense absorption peaks emerge, reflecting the higher density of accessible electronic states. Finally, Region IV (24.0–32.0 eV), highlighted in beige, delineates the high–energy regime in which the maximum absorption peak occurs, characteristic of transitions involving deeper electronic states. The colored curves correspond to the different crystallographic orientations considered, whereas the black curve represents the polycrystalline response, enabling the evaluation of the optical anisotropy of the material.

Experimental studies related to the optical absorption of $CaSO_4$ have found peaks in the UV region. For example, one study reported an absorption maximum of around 325 nm (~ 3.81 eV), while another reported absorption near 280 nm (~ 4.43 eV) [47]. The simulated absorption peaks in our work, ranging from 10 to 29 eV, are higher than these experimental values. This difference can be attributed to the fact that simulations capture electronic transitions, including higher-energy excitations, which may not be directly observed in conventional UV spectroscopy. Nonetheless, the computational spectra provide complementary insights into the electronic structure and optical behavior of orthorhombic $CaSO_4$. We believe that the combination of experimental data and simulated spectra strengthens the reliability and interpretability of our results. The curves for the different directions are very close (see Fig. 4). The orthorhombic $CaSO_4$ has low optical anisotropy, meaning that the absorption is practically isotropic. The absorption coefficient (η) can be expressed by the equation $\eta = 2k\omega/c$, where η quantifies the fraction of energy lost by the electromagnetic wave as it propagates through the material [43].

Fig. 5 shows the real and imaginary parts of the complex dielectric function of orthorhombic $CaSO_4$, $\varepsilon(\omega) = \varepsilon_1(\omega) + i\varepsilon_2(\omega)$, where ($\varepsilon_1(\omega)$, blue) and ($\varepsilon_2(\omega)$, magenta) represent the real and imaginary components, respectively. The calculations were performed using the GGA–PBEsol functional for photon energies ranging from 0 to 35 eV. The static dielectric constant inferred from is $\varepsilon_1(0) \approx 2.8$, corresponding to a low-energy refractive index of $n_0 \approx \sqrt{\varepsilon_1(0)} \approx 1.67$ [53]. Below

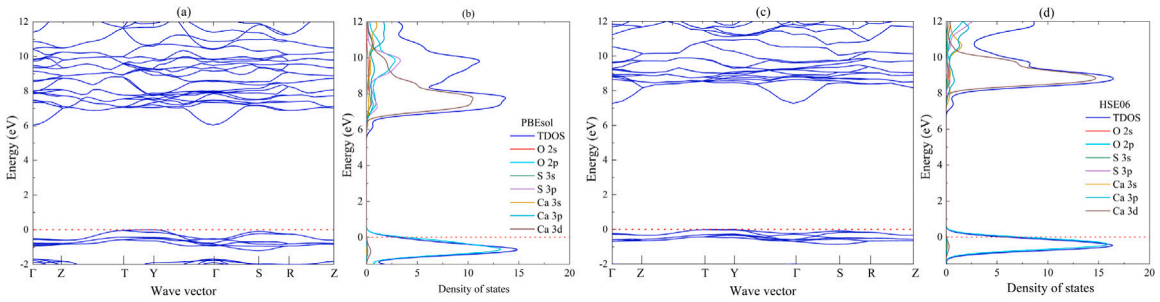

Fig. 3. Electronic band structures (left panels) and total + projected density of states (right panels) for orthorhombic $CaSO_4$ computed with (a,b) PBEsol and (c,d) HSE06. The red dashed line denotes the Fermi level (0 eV).

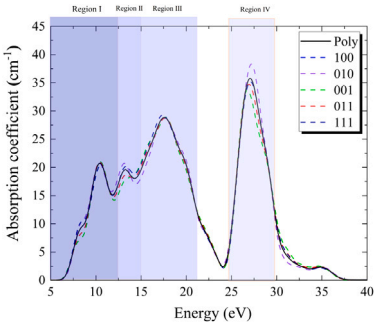

Fig. 4. Optical absorption coefficient of orthorhombic $CaSO_4$ as a function of energy when incident UV light is polarized along the crystalline planes and for a polycrystalline (poly) sample.

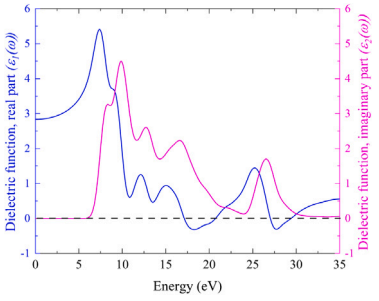

Fig. 5. Dielectric function of $CaSO_4$ vs energy.

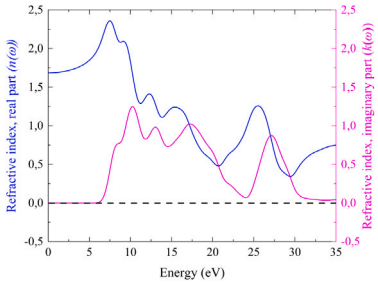

Fig. 6. Refractive index of $CaSO_4$ vs photon energy.

approximately 8.0 eV, $\varepsilon_2(\omega)$ remains essentially zero, indicating the absence of interband absorption and confirming the wide-bandgap insulating nature of $CaSO_4$. A pronounced absorption band appears around 9.0–11.0 eV, where $\varepsilon_2(\omega)$ reaches its main peak; this feature is attributed to strong (O, 2p→Ca, 3d) interband transitions, as corroborated by the PDOS analysis. Secondary spectral features between 15.0 and 25.0 eV originate from transitions involving deeper valence states (O 2*s*, S 3*s*). The dispersion of $\varepsilon_1(\omega)$ near the absorption peaks follows the causality principle described by the Kramers–Kronig relations [54]. Finally, the region where $\varepsilon_1(\omega)$ approaches zero, around 18.0–22.0 eV, suggests the possible occurrence of a bulk plasmon resonance. Notably, $\varepsilon_1(\omega)$ remains positive up to approximately 26.0–27.0 eV and crosses zero near the plasma energy; this behavior indicates a transition from a typical dielectric to a reflective (metal-like) response at higher photon energies. Overall, the calculated dielectric response confirms that $CaSO_4$ is optically transparent in the visible range, with low $k(\omega)$ and $n_0 \sim 1.67$, while exhibiting strong ultraviolet absorption bands associated with interband electronic excitations.

Fig. 6 shows the complex refractive index of orthorhombic $CaSO_4$ as functions of the photon energy (in eV), calculated using the GGA–PBEsol functional, given by $\tilde{n}(\omega) = n(\omega) + i\,k(\omega)$, where $n(\omega)$ and $k(\omega)$ are the real and imaginary parts, respectively. The real part ($n(\omega)$, blue) describes the phase velocity of light in the medium, whereas the imaginary part ($k(\omega)$, magenta) represents the extinction coefficient associated with optical absorption. At low photon energies (below approximately 8.0 eV), $k(\omega)$ remains nearly zero, indicating the absence of interband absorption and confirming the wide-bandgap insulating character of $CaSO_4$. In this region, the static refractive index is approximately $n_0 \approx 1.67$, consistent with the expected transparency in the visible range [55]. It is important to emphasize that, from an experimental standpoint, synthesized $CaSO_4$ typically exhibits an opaque appearance. However, in the experimental study conducted by Huang et al. (2024) [55], the authors reported that the refractive index decreases linearly with the reduction of water content, reaching a value of 1.85 for anhydrous $CaSO_4$ with a sample thickness of 0.03 mm. This value is slightly higher than that obtained from the first-principles calculations performed in this work ($\Delta = 0.18$). Such a discrepancy can be attributed to factors such as sample thickness and structural imperfections, including edge effects, finite crystallite size, and lattice strain, which are not accounted for in the theoretical simulations. The first pronounced absorption band appears between 9.0 and 11.0 eV, where both $k(\omega)$ and $n(\omega)$ display intense peaks, reaching about 1.0 and 2.4, respectively. These peaks are attributed to strong interband transitions, mainly from O 2*p* to Ca 3*d* orbitals, as indicated by the PDOS analysis.

Fig. 7 shows the complex optical conductivity as functions of the photon energy (in eV), calculated using the GGA–PBEsol functional. Below 5.0 eV, no significant absorption occurs, confirming transparency below the bandgap, $E_g = 6.044$ eV and $E_g = 7.271$ eV. The real part, ($\sigma_1(\omega)$, violet) represents direct absorption, and exhibits multiple peaks between 5.0 and 35.0 eV, associated with interband transitions. The imaginary part, ($\sigma_2(\omega)$, magenta) describes dispersive effects and energy storage, with alternating positive and negative peaks linked to resonance. A pronounced peak appears near 28.0 eV, probably of plasmonic origin. Above 35.0 eV, the optical response decreases

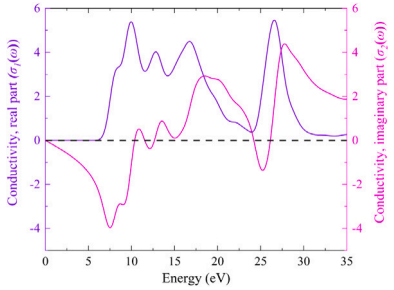

Fig. 7. Optical conductivity of $CaSO_4$ vs photon energy.

sharply. Overall, Fig. 7 shows that orthorhombic $CaSO_4$ has a complex and anisotropic optical response, with regions of strong absorption linked to electronic transitions.

In summary, orthorhombic $CaSO_4$ exhibits a complex and partially anisotropic optical response, with well-defined absorption features directly related to its electronic structure. These characteristics are essential for understanding its dielectric and plasmonic properties and for guiding its use in optoelectronic and UV/visible applications.

3.5. Elastic properties

The mechanical properties of a crystalline system is governed by its elastic constant, which reflect the resistance of the material to deformation under external forces. For orthorhombic crystals, there are nine independent elastic constants: C_{11}, C_{22}, C_{33} C_{44}, C_{55}, C_{66}, C_{12}, C_{13}, and C_{23}. Larger values of the elastic constants (C_{ij}) indicate greater resistance of the lattice to applied mechanical stress [56,57]. Specifically, C_{11}, C_{22}, and C_{33} correspond to the uniaxial compressive strength along the *a*, *b*, and *c* crystallographic axes, respectively, whileC_{44}, C_{55}, and C_{66} represent the shear resistance along the (100), (010), and (001) crystallographic planes, respectively. The calculated values C_{ij} for orthorhombic $CaSO_4$ (space group *Cmcm*) satisfy the Born–Huang mechanical stability conditions [57–60]:

$$C_{ij} > 0, \tag{2a}$$

$$C_{11} + C_{22} + C_{33} + 2(C_{12} + C_{13} + C_{23}) > 0, \tag{2b}$$

$$C_{11} + C_{22} - 2C_{12} > 0, \tag{2c}$$

$$C_{11} + C_{33} - 2C_{13} > 0, \tag{2d}$$

$$C_{22} + C_{33} - 2C_{23} > 0. \tag{2e}$$

Table 4 shows the elastic constants (C_{ij}) and elastic compliance matrix (S_{ij}) for orthorhombic $CaSO_4$. Of the axial constants, C_{33} is the largest (168.29 GPa), while C_{11} is the smallest, confirming elastic anisotropy. For the shear modes, C_{55} (12.52 GPa) is significantly smaller than C_{44} and C_{66}, indicating low resistance to wear in this direction. The calculated values of the elastic constants for orthorhombic $CaSO_4$ (Table 4) reveal significant anisotropy, particularly in the shear plane associated with C_{55} = 12.52 GPa, a value that is substantially lower than C_{44} = 39.78 GPa and C_{66} = 36.43 GPa. This reduced value indicates that the material is more easily deformable by shear along the plane corresponding to C_{55}, suggesting higher compressibility and susceptibility to deformation in this specific crystallographic direction. In contrast, the higher values of C_{44} and C_{66} indicate greater resistance to shear deformations in the respective planes, highlighting the mechanical anisotropy of orthorhombic $CaSO_4$. These characteristics can significantly influence the structural stability and mechanical performance of the material in applications where directional or shear stresses are predominant. The large value of the compliance constant S_{55} reinforces this result, indicating that the crystal is particularly susceptible to shear deformation along the corresponding plane. Negative off-diagonal elements in S_{ij} are physically meaningful, as they reflect the usual coupling in which stress in one direction induces contraction in another.

Table 4
Elastic constants (C_{ij}) and non-zero elastic compliance coefficients (S_{ij}) for orthorhombic $CaSO_4$.

Orthorhombic $CaSO_4$			
C_{ij}	Value (GPa)	S_{ij}	Value (10^{-3} GPa^{-1})
C_{11}	127.59	S_{11}	0.00864
C_{12}	40.38	S_{12}	−0.00245
C_{13}	15.76	S_{13}	−0.00018
C_{22}	139.04	S_{22}	0.00850
C_{23}	42.90	S_{23}	−0.00194
C_{33}	168.29	S_{33}	0.00645
C_{44}	39.78	S_{44}	0.02513
C_{55}	12.52	S_{55}	0.07985
C_{66}	36.43	S_{66}	0.02745

The elastic modulus is derived from the elastic constants using the Voigt–Reuss–Hill (VRH) scheme. For orthorhombic $CaSO_4$ crystals, the bulk modulus (B) and shear modulus (G) according to the Voigt (V), Hill (H) and Reuss (R) approximations are obtained as follows [57,61]:

$$B_V = \frac{1}{9}(C_{11} + C_{22} + C_{33}) + \frac{2}{9}(C_{12} + C_{13} + C_{23}), \tag{3a}$$

$$G_V = \frac{1}{15}(C_{11} + C_{22} + C_{33}) - \frac{1}{15}(C_{12} + C_{13} + C_{23}) + \frac{1}{5}(C_{44} + C_{55} + C_{66}), \tag{3b}$$

$$B_R = \Delta[a + b]^{-1}, \tag{3c}$$

$$G_R = 15\left[\frac{4(d - e)}{\Delta + \left(\frac{3}{C_{44}} + \frac{3}{C_{55}} + \frac{1}{C_{66}}\right)}\right]^{-1}, \tag{3d}$$

$$a = C_{11}(C_{22} + C_{33} - 2C_{23}) + C_{22}(C_{33} - 2C_{13}) - 2C_{33}C_{12}, \tag{3e}$$

$$b = C_{12}(2C_{23} - C_{12}) + C_{13}(2C_{12} - C_{13}) + C_{23}(2C_{13} - C_{23}), \tag{3f}$$

$$d = C_{11}(C_{22} + C_{33} + C_{23}) + C_{22}(C_{33} + C_{13}) + C_{33}C_{12}, \tag{3g}$$

$$e = C_{12}(C_{23} + C_{12}) + C_{13}(C_{12} + C_{13}) + C_{23}(C_{13} + C_{23}), \tag{3h}$$

$$\Delta = C_{13}(C_{12}C_{23} - C_{13}C_{22}) + C_{23}(C_{12}C_{13} - C_{23}C_{11}) + C_{33}(C_{11}C_{22} - C_{12}^2). \tag{3i}$$

Hill [57] demonstrated that the Voigt and Reuss equations provide upper and lower bounds, respectively, for the polycrystalline constants, and recommended an arithmetic mean as a practical estimate. Thus, the bulk modulus (B), shear modulus (G), Young's modulus (Y), and Poisson's ratio (ν) are obtained as [57,60]:

$$B = \frac{B_V + B_R}{2}, \tag{4a}$$

$$G = \frac{G_V + G_R}{2}, \tag{4b}$$

$$Y = \frac{9BG}{3B + G}, \tag{4c}$$

$$\nu = \frac{3B - Y}{6B}. \tag{4d}$$

All known crystalline materials exhibit elastic anisotropy, and an accurate description is crucial for applications in solid-state physics and engineering. The universal anisotropy index (A^U), the percentage anisotropy (A_G), the bulk anisotropy (A_B), and the shear anisotropy factor (A_1, A_2, A_3) can be used to quantify this behavior [57]:

$$A^U = \frac{5G_V}{G_R} + \frac{B_V}{B_R} - 6, \tag{5a}$$

$$A_G = \frac{G_V - G_R}{G_V + G_R}, \tag{5b}$$

$$A_B = \frac{B_V - B_R}{B_V + B_R}, \tag{5c}$$

$$A_1 = \frac{4C_{44}}{C_{11} + C_{33} - 2C_{13}}, \tag{5d}$$

$$A_2 = \frac{4C_{55}}{C_{22} + C_{33} - 2C_{23}}, \tag{5e}$$

$$A_3 = \frac{4C_{66}}{C_{11} + C_{22} - 2C_{12}}. \tag{5f}$$

The calculated anisotropy indices for orthorhombic $CaSO_4$ indicate a moderate degree of elastic anisotropy. The universal anisotropy index is $A^U \approx 1.84$ the percentage anisotropy of the shear modulus is $A_G \approx 15.4\%$, and the bulk modulus anisotropy is $A_B \approx 0.8\%$, indicating nearly isotropic resistance to uniform compression. The shear anisotropy factors are $A_1 = 0.60$, $A_2 = 0.23$, and $A_3 = 0.78$, with A_2 the lowest and A_3 the highest. Overall, orthorhombic $CaSO_4$ exhibits nearly isotropic compressive behavior but pronounced directional variation in shear properties, which may affect its mechanical performance in specific crystallographic orientations. Titanium–aluminum–nitride alloy ($Ti_{0.8}Al_{0.2}N$) has values of $A^U \sim 2.0$, $A_G \sim 20\%$, and $A_B \sim 5.0\%$, indicating high anisotropy. This material is widely used in hard coatings due to its high wear resistance; however, its pronounced anisotropy increases its susceptibility to fracture failure in specific directions. Hafnium dioxide (HfO_2), with values of $A^U \sim 1.3$, $A_G \sim 10.0\%$, and $A_B \sim 3.0\%$, exhibits relatively low anisotropy, favoring mechanical uniformity and structural stability, which are essential characteristics for electronic and dielectric devices [62]. Oxides of magnesium (MgO), cobalt (CoO), nickel (NiO), copper (CuO), and zinc (ZnO) exhibit minimal anisotropy ($A^U \sim 1.1$, $A_G \sim 5.0\%$, $A_B \sim 2.0\%$), and are practically isotropic. This characteristic is desirable in applications requiring mechanical uniformity, such as sensors and optoelectronic devices [63]. Compared to these materials, $CaSO_4$ combines moderate anisotropy with stable mechanical properties, making it suitable for thin coating applications where there are no critical directional stresses. Its performance lies between that of high–anisotropy materials, such as $Ti_{0.8}Al_{0.2}N$, and nearly isotropic materials, such as HfO_2 and (Mg, Co, Ni, Cu, Zn)O, thereby offering a balance between mechanical strength and structural reliability.

Table 5 shows that Pugh's ratios (B/G), calculated using the Voigt, Reuss, and Hill approaches, are 1.75, 2.35, and 2.01, respectively. Since the Reuss and Hill values exceed the critical threshold of 1.75 [60,64], which is typically used to distinguish ductile from brittle behavior, orthorhombic $CaSO_4$ is expected to exhibit predominantly ductile mechanical behavior. The estimated value for the Vickers hardness of $H_V \approx 3.9$ GPa suggests that orthorhombic $CaSO_4$ is a relatively soft material. The calculated bulk modulus ($B = 69.8$ GPa) and the estimated hardness are consistent with the typical mechanical behavior of wide-bandgap ionic insulators. To validate these results, we compared them with available experimental data for the two main phases of calcium sulfate: gypsum ($CaSO_4 \cdot 2H_2O$) and anhydrite ($CaSO_4$). For gypsum, neutron diffraction measurements gave a bulk modulus of 45 ± 1 GPa [65], while first-principles calculations yielded a value of approximately 49.0 GPa for the stable gypsum-I phase [66]. In contrast, experimental studies of anhydrite have consistently reported higher values for the stiffness, with bulk moduli in the range 82.0–83.0 GPa [67,68]. Our calculated value of $B = 69.8$ GPa lies between the experimental ranges for gypsum and anhydrite, showing good consistency with the literature and confirming the relatively soft mechanical properties of orthorhombic $CaSO_4$.

To enable a detailed analysis of the elastic anisotropy of orthorhombic CaSO4, Figs. 8(a-d) present the elastic modulus patterns, showing four fundamental properties in both 3D and 2D projections (xy, xz, and yz planes). These figures show the maximum and minimum variations of Young's modulus (Y), linear compressibility (β), shear modulus (G), and Poisson's ratio (ν), calculated using the GGA-PBEsol exchange–correlation functional at a pressure of 0 GPa. The results confirm strong anisotropy in (Y), (G), and (ν), while β, remains the most isotropic property. This variation is fully consistent with the orthorhombic symmetry, which allows for different mechanical responses along each crystallographic axis. Such pronounced anisotropies may influence the material's behavior in structural applications or under directional stress.

Table 5
Elastic moduli and derived mechanical properties of orthorhombic $CaSO_4$ (at 0 GPa).

Property	Voigt	Reuss	Hill
Bulk modulus B	70.34	69.23	69.79
Shear modulus G	40.14	29.41	34.78
Young's modulus Y	101.18	77.30	89.47
Lame's first parameter λ	43.58	49.62	46.60
Poisson's ratio ν	0.260	0.314	0.286
Hardness H	4.48	3.37	3.93
Pugh ratio B/G	1.75	2.35	2.01

Table 6
Anisotropy values and minimum and maximum ranges for elastic moduli for orthorhombic $CaSO_4$.

Parameter	Symbol	$CaSO_4$
Young's Modulus (GPa)	Y_{min}	42.26
	Y_{max}	154.96
	A	3.66
Linear Compressibility	β_{min}	4.11
	β_{max}	6.00
	A	1.45
Shear Modulus (GPa)	G_{min}	12.52
	G_{max}	64.69
	A	5.16
Poisson's Ratio	ν_{min}	−0.03
	ν_{max}	0.71
	A	∞

Table 6 summarizes the maximum-to-minimum ratios of Y_{max}, β_{max}, G_{max}, and ν_{max}, together with anisotropy factors, reinforcing that Young's and shear moduli are the most anisotropic properties. Poisson's ratio exhibits unusual behavior, including a negative minimum value and infinite anisotropy, indicating strong directional dependence. In contrast, linear compressibility remains relatively isotropic.

Finally, the wide-bandgaps of 6.044 eV (PBEsol) and 7.271 eV (HSE06), obtained from calculations of the electronic band structure and the total + projected density of states, indicate a predominantly ionic character of the Ca^{2+}-SO_4^{2-} bond. This strong electrostatic interaction results in high phonon frequencies, particularly in optical modes, reflecting the rigidity of the crystal lattice. The combination of electronic and vibrational characteristics explains the favorable mechanical behavior of orthorhombic $CaSO_4$, including a high Young's modulus, moderate hardness, and limited ductility typical characteristics of structural ceramics, insulating materials, and mechanically stable substrates.

4. Conclusion

This paper has presented a comprehensive theoretical investigation of the physical properties of orthorhombic $CaSO_4$ using DFT. Structural optimization was performed with the LDA, PBE, PBEsol exchange–correlation functionals, while the screened hybrid HSE06 functional was employed to refine the electronic structure, yielding a bandgap of $E_g = 7.271$ eV compared to the value of $E_g = 6.044$ eV obtained with PBEsol. When taken together, the results for the negative total energy, cohesive energy, and phonon dispersion demonstrate robust structural stability and strong interatomic bonding. The Born–Huang mechanical stability criteria, together with the calculated elastic constants, confirm the mechanical stability of the $CaSO_4$ crystal and reveal anisotropic responses to shear, particularly along specific crystallographic planes

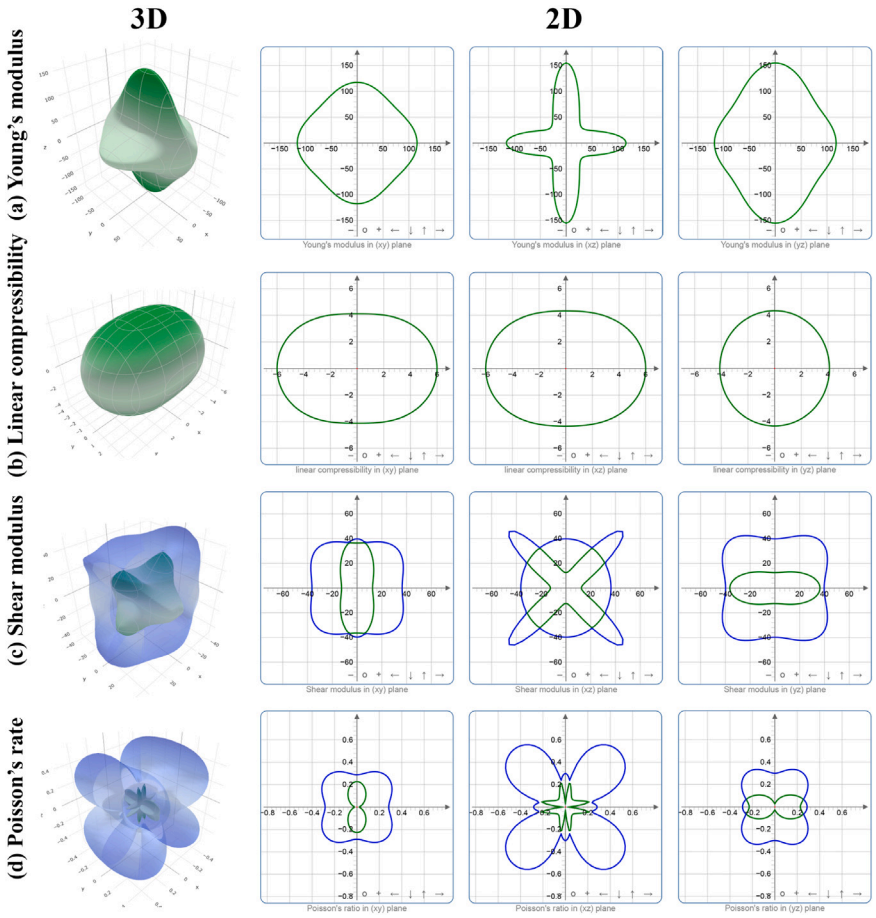

Fig. 8. Plots of 3D and 2D elastic moduli for orthorhombic $CaSO_4$.

such as (010) and (100), where differential elastic stiffness is most pronounced. In addition, an optical analysis shows polarization-dependent absorption in the UV region while maintaining nearly isotropic behavior. In summary, these findings advance the current understanding of the fundamental physical properties of $CaSO_4$ and support its potential application as a stable insulating and optoelectronically relevant material.

CRediT authorship contribution statement

Marcelo F.S. Santos: Writing – review & editing, Visualization, Validation, Investigation, Formal analysis, Data curation, Conceptualization. **Carlos H.P. Silva:** Writing – review & editing, Writing – original draft, Validation, Software, Resources, Methodology, Funding acquisition, Formal analysis, Data curation. **Ivana M.G.A. Cavalcanti:** Writing – review & editing, Visualization, Investigation, Data curation. **Danilo O. Junot:** Writing – review & editing, Visualization, Investigation, Formal analysis, Data curation. **Anderson M.B. Silva:** Writing – review & editing, Visualization, Investigation, Formal analysis, Data curation. **Marcos V.S. Rezende:** Writing – review & editing, Writing – original draft, Visualization, Supervision, Investigation, Formal analysis, Data curation, Conceptualization. **Érico R.P. Novais:** Writing – review & editing, Visualization, Validation, Software, Investigation, Formal analysis, Data curation, Conceptualization. **Linda V.E. Caldas:** Writing – review & editing, Visualization, Investigation, Funding acquisition, Formal analysis, Data curation. **Andréa L.F. Novais:** Writing – review & editing, Writing – original draft, Visualization, Supervision, Methodology, Investigation, Formal analysis, Data curation, Conceptualization. **Divanizia N. Souza:** Writing – review & editing, Visualization, Supervision, Investigation, Formal analysis, Data curation, Conceptualization.

Generative AI and AI-assisted technologies in the writing process statement

During the preparation of this work, the author(s) used ChatGPT (OpenAI), available at https://chat.openai.com, to enhance the language and readability of the text. After using this tool, the author(s) reviewed and edited the content as necessary and assume full responsibility for the final content of this manuscript.

Declaration of competing interest

We confirm that this work is original and has not been published previously nor is it under consideration for publication elsewhere. All authors declare that they have no competing financial or personal relationships that could have influenced the work reported in this paper.

Acknowledgments

The authors are grateful to FINEP (Brazilian Innovation Agency), CAPES (Brazilian Federal Agency, for financing the first author Marcelo Franklin da S. Santos), CNPq (No. 306229/2023-4; 405536/2023-2; 307008/2022-3; 406761/2022–1; 305142/2021-6), FAPESP (No. 2018/05982–0 and 2023/04859-8), National Institute of Radiation Technology in Health Science (INTERAS) (Brazilian National Council for Scientific and Technological Development), CENAPAD (National High Performance Processing Center in São Paulo), and FUNAPE (Research Support Foundation). We thank the Coaraci Supercomputer for computer time (FAPESP grant 2019/17874-0) and the Center for Computing in Engineering and Sciences at UNICAMP (FAPESP grant 2013/08293-4).

Data availability

Data will be made available on request.

References

[1] Y. Wang, X. Mao, C. Chen, W. Wang, W. Dang, Effect of sulfuric acid concentration on morphology of calcium sulfate hemihydrate crystals, Mater. Res. Express 7 (10) (2020) 105501, http://dx.doi.org/10.1088/2053-1591/abbc41.

[2] M.V. Thomas, D.A. Puleo, M. Al-Sabbagh, Calcium sulfate: A review, J. Long-Term Eff. Med. Implant. 15 (6) (2005) 599–607, http://dx.doi.org/10.1615/JLongTermEffMedImplants.v15.i6.30.

[3] W. Liu, C. Wu, W. Liu, W. Zhai, J. Chan, The effect of plaster ($caso_4 \cdot 1/2h_2o$) on the compressive strength, self-setting property, and in vitro bioactivity of silicate-based bone cement, J. Biomed. Mater. Res. Part B: Appl. Biomater. 101B (2) (2013) 279–286, http://dx.doi.org/10.1002/jbm.b.32837.

[4] T.T. Yan, S.Y. Wu, M. Fang, Q.H. Chen, Research of preparation and properties of $caso_4$/haw bone graft substitute, Appl. Mech. Mater. 707 (2014) 154–157, http://dx.doi.org/10.4028/www.scientific.net/amm.707.154.

[5] M.A.A. Zahari, S.P. Lee, S.R. Kasim, Synthesis of calcium sulphate as biomaterial, AIP Conf. Proc. 2267 (1) (2020) 020081, http://dx.doi.org/10.1063/5.0015693.

[6] J. Qi, H. Zhu, P. Zhou, X. Wang, Z. Wang, S. Yang, D. Yang, B. Li, Application of phosphogypsum in soilization: a review, Int. J. Environ. Sci. Technol. 20 (9) (2023) 10449–10464, http://dx.doi.org/10.1007/s13762-023-04783-2.

[7] Y. Ennaciri, M. Bettach, The chemical behavior of the different impurities present in phosphogypsum: a review, Phosphorus Sulfur Silicon Relat. Elem. 199 (2) (2024) 129–148, http://dx.doi.org/10.1080/10426507.2023.2281489.

[8] F.C.B. Zambrosi, L.R.F. Alleoni, E.F. Caires, Aplicação de gesso agrí cola e especiação iônica da solução de um latossolo sob sistema plantio direto, Ciência Rural. 37 (1) (2007) 110–117, http://dx.doi.org/10.1590/S0103-84782007000100018.

[9] S. Bastani, L. Oliveira, E. Yukihara, Development and characterization of lanthanide-doped caso4 for temperature sensing applications, Opt. Mater. 92 (2019) 273–283, http://dx.doi.org/10.1016/j.optmat.2019.04.022.

[10] A. Silva, D. Souza, L. Caldas, Thermoluminescence and optically stimulated luminescence of caso4:mn, tb with different dopant concentrations, Radiat. Phys. Chem. 237 (2025) 113032, http://dx.doi.org/10.1016/j.radphyschem.2025.113032.

[11] A. Castro-Campoy, C. Cruz-Vázquez, R. Pérez-Salas, V. Castaño, R. Bernal, Novel non-thermoluminescent caso4:dy dosimeters, Appl. Radiat. Isot. 217 (2025) 111606, http://dx.doi.org/10.1016/j.apradiso.2024.111606.

[12] V. Guckan, S. Bereket, V. Altunal, W. Abusaid, Z. Yegingil, Luminescence properties of tb and eu activated caso4 phosphor, Radiat. Phys. Chem. 203 (2023) 110620, http://dx.doi.org/10.1016/j.radphyschem.2022.110620, https://www.sciencedirect.com/science/article/pii/S0969806X22006831.

[13] F. L. A., C . Viccari, P. Nicolucci, Dosimetric properties of thermoluminescent pellets of $caso_4$ doped with rare earths at low doses, Radiat. Phys. Chem. 171 (2020) 108704, http://dx.doi.org/10.1016/j.radphyschem.2020.108704.

[14] A.M.B. Silva, D.S. Rodrigues, B.D.O. Guedes, I.S. Silveira, P.L. Antonio, D.O. Junot, L.V.E. Caldas, D.N. Souza, Exploring the luminescence properties and dosimetric characteristics of $caso_4$:tb, $caso_4$:mn, and $caso_4$:mn, tb phosphors synthesized by slow evaporation route, Radiat. Meas. 177 (2024) http://dx.doi.org/10.1016/j.radmeas.2024.107261.

[15] A.M.B. Silva, L.F. Souza, P.L. Antonio, D.O. Junot, L.V.E. Caldas, D.N. Souza, Effects of manganese and terbium on the dosimetric properties of $caso_4$, Radiat. Phys. Chem. 198 (2022) 110207, http://dx.doi.org/10.1016/j.radphyschem.2022.110207.

[16] S. Mohamed, E. Salama, H.A. Alazab, A. Bakry, A. Sharma, Y. Assran, Synthesis and characterization of high-sensitivity dy, eu co-doped $caso_4$ thermoluminescent phosphor using coprecipitation technique, Luminescence 39 (1) (2024) 1–7, http://dx.doi.org/10.1002/bio.4679.

[17] A.I. Castro-Campoy, R. Bernal, C. Cruz-Vázquez, V.R. Orante-Barrón, A.R. García-Haro, V.E. Alvarez-Montaño, Synthesis and thermoluminescence characterization of self-agglomerating caso4 exposed to beta radiation, Appl. Radiat. Isot. 148 (2019) 76–79, http://dx.doi.org/10.1016/j.apradiso.2019.03.024.

[18] D.O. Junot, D.C. Galeano, A.M.B. Silva, D.N. Souza, L.V.E. Caldas, Development of caso4:re,li (re = tm, eu, tb) composites for thermally or optically stimulated luminescence dosimetry, Radiat. Meas. 176 (2024) 107217, http://dx.doi.org/10.1016/j.radmeas.2024.107217.

[19] D.O. Junot, J.P. Barros, L.V.E. Caldas, D.N. Souza, Thermoluminescent analysis of caso4:tb, eu crystal powder for dosimetric purposes, Radiat. Meas. 90 (2016) 228–232, http://dx.doi.org/10.1016/j.radmeas.2016.01.020.

[20] T. Yamashita, N. Nada, H. Onishi, S. Kitamura, Calcium sulfate activated by thulium or dysprosium for thermoluminescence dosimetry, Health Phys. 21 (2) (1971) 295–300, http://dx.doi.org/10.1097/00004032-197108000-00016.

[21] R. Rani, A. Lakshmanan, V. Sivakumar, R. Venkatasamy, O. Annalakshmi, M. Jose, K. Marimuthu, Redox and charge transfer processes and luminescence in caso4:zn, mn, Radiat. Meas. 76 (2015) 8–16, http://dx.doi.org/10.1016/j.radmeas.2015.03.001.

[22] A. Kadari, K. Mahi, R. Mostefa, M. Badaoui, A. Mameche, D. Kadri, Optical and structural properties of mn doped caso4 powders synthesized by sol–gel process, J. Alloys Compd. 688 (2016) 32–36, http://dx.doi.org/10.1016/j.jallcom.2016.07.040.

[23] N. Salah, P.D. Sahare, S.P. Lochab, P. Kumar, Tl and pl studies on caso4: Dy nanoparticles, Radiat. Meas. 41 (1) (2006) 40–47, http://dx.doi.org/10.1016/j.radmeas.2005.07.026.

[24] M. Zahedifar, M. Mehrabi, S. Harooni, Synthesis of caso4: Mn nanosheets with high thermoluminescence sensitivity, Appl. Radiat. Isot. 69 (7) (2011) 1002–1006, http://dx.doi.org/10.1016/j.apradiso.2011.01.036.

[25] C. Jia, L. Wu, J. Fulton, X. Liang, J. Yoreo, B. Guan, Structural characteristics of amorphous calcium sulfate: Evidence to the role of water molecules, J. Phys. Chem. C 125 (2021) http://dx.doi.org/10.1021/acs.jpcc.0c10016.

[26] K. Baolin, Z. Qin, L. Xianhai, S. Zhihui, Adsorption and solidification of cadmium by calcium sulfate dihydrate (gypsum) in an aqueous environment: a dispersion-corrected dft and ab initio molecular dynamics study, Phys. Chem. Chem. Phys. 24 (2022) 9521–9533, http://dx.doi.org/10.1039/D1CP03964D.

[27] D. Kong, B. Nie, Y. Zhang, Q. Chen, N. An, N. He, L. Yao, Y. Zhai, A comprehensive understanding of the role of sodium sulfate in calcium looping via in-situ experiments and dft studies: Performance and mechanism, Fuel 371 (2024) 131968, http://dx.doi.org/10.1016/j.fuel.2024.131968.

[28] C. Santos, C. Silva, M. Santos, E. Novais, D. Souza, M. Rezende, A. Novais, Dft to study the structural, optoelectronic and mechanical properties of cunipd and cu2ppd2 alloys, J. Alloys Compd. 1038 (2025) 182830, http://dx.doi.org/10.1016/j.jallcom.2025.182830.

[29] M. Segall, P. Lindan, M. Probert, C. Pickard, P. Hasnip, S. Clark, M. Payne, First–principles simulation: ideas, illustrations and the castep code, J. Phys.: Condens. Matter. 14 (11) (2002) 2717–2744, http://dx.doi.org/10.1088/0953-8984/14/11/301.

[30] P. Hohenberg, W. Kohn, Inhomogeneous electron gas, Phys. Rev. 136 (1964) B864–B871, http://dx.doi.org/10.1103/PhysRev.136.B864.

[31] Materials data on caso4 by materials project, 2020, http://dx.doi.org/10.17188/1208130.

[32] W. Kohn, L.J. Sham, Self-consistent equations including exchange and correlation effects, Phys. Rev. 140 (1965) A1133–A1138, http://dx.doi.org/10.1103/PhysRev.140.A1133, https://link.aps.org/doi/10.1103/PhysRev.140.A1133.

[33] J.P. Perdew, A. Zunger, Self-interaction correction to density-functional approximations for many-electron systems, Phys. Rev. B 23 (10) (1981) 5048–5079, http://dx.doi.org/10.1103/PhysRevB.23.5048.

[34] J.P. Perdew, K. Burke, M. Ernzerhof, Generalized gradient approximation made simple, Phys. Rev. Lett. 77 (18) (1996) 3865–3868, http://dx.doi.org/10.1103/PhysRevLett.77.3865.

[35] J.P. Perdew, A. Ruzsinszky, G.I. Csonka, O.A. Vydrov, G.E. Scuseria, L.A. Constantin, X. Zhou, K. Burke, Restoring the density-gradient expansion for exchange in solids and surfaces, Phys. Rev. Lett. 100 (13) (2008) 136406, http://dx.doi.org/10.1103/PhysRevLett.100.136406.

[36] J. Heyd, G.E. Scuseria, M. Ernzerhof, Hybrid functionals based on a screened coulomb potential, J. Chem. Phys. 118 (18) (2003) 8207–8215, http://dx.doi.org/10.1063/1.1564060.

[37] A.V. Krukau, O.A. Vydrov, A.F. Izmaylov, G.E. Scuseria, Influence of the exchange screening parameter on the performance of screened hybrid functionals, J. Chem. Phys. 125 (22) (2006) 224106, http://dx.doi.org/10.1063/1.2404663.

[38] H.J. Monkhorst, J.D. Pack, Special points for brillouin-zone integrations, Phys. Rev. B 13 (1976) 5188–5192, http://dx.doi.org/10.1103/PhysRevB.13.5188.

[39] B.G. Pfrommer, M. Côté, S.G. Louie, M.L. Cohen, Relaxation of crystals with the quasi-Newton method, J. Comput. Phys. 131 (1997) 233–240, http://dx.doi.org/10.1006/jcph.1996.5612.

[40] R. Gaillac, P. Pullumbi, F.-X. Coudert, ELATE: an open-source online application for analysis and visualization of elastic tensors, J. Phys.: Condens. Matter. 28 (27) (2016) 275201, http://dx.doi.org/10.1088/0953-8984/28/27/275201.

[41] W.D.B.P. Schweiss, H. Fuess, A theoretical lattice dynamics model and phonon dispersion measurements for $caso_4$ (anhydrite), J. Phys. C: Solid State Phys. 20 (5) (1987) 651–664, http://dx.doi.org/10.1088/0022-3719/20/5/004.

[42] D. Korabel'nikov, Y.N. Zhuravlev, Structural, elastic, electronic and vibrational properties of a series of sulfates from first principles calculations, J. Phys. Chem. Solids 119 (2018) 114–121, http://dx.doi.org/10.1016/j.jpcs.2018.03.037.

[43] F. Moucherek, W. Santos, A. Novais, E. Moreira, D. Azevedo, Prediction of electronic and optical properties of monoclinic 1t'-phase $osse_2$ monolayer using dft principles, Mater. Today Commun. 33 (2022) 104764, http://dx.doi.org/10.1016/j.mtcomm.2022.104764.

[44] W. Santos, A. Santos, F. Ferreira, E. de Novais, A. Rodrigues, N. Frazão, A. Novais, D. Souza, Understanding the optoelectronic and vibrational properties of mb_4o_7, using density functional theory, where m=yb or ce, Opt. Mater. 157 (2024) 116210, http://dx.doi.org/10.1016/j.optmat.2024.116210.

[45] L. Gracia, A. Beltrán, D. Errandonea, J. Andrés, Caso4 and its pressure-induced phase transitions: A density functional theory study, Inorg. Chem. 51 (3) (2011) 1751–1759, http://dx.doi.org/10.1021/ic202056b.

[46] J. Shi, J. Zhang, L. Yang, M. Qu, D.-C. Qi, K.H.L. Zhang, Wide bandgap oxide semiconductors: from materials physics to optoelectronic devices, Adv. Mater. 33 (50) (2021) 2006230.

[47] H. Nagabhushana, G. Nagaraju, B. Nagabhushana, C. Shivakumara, R. Chakradhar, Hydrothermal synthesis and characterization of caso4 pseudomicrorods, Phil. Mag. Lett. 90 (4) (2010) 289–298, http://dx.doi.org/10.1080/09500831003636051.

[48] Z.M. Salikhodzha, T.N. Nurakhmetov, A.T. Akilbekov, A.M. Zhunusbekov, A.Z. Kainarbay, B.M. Sadykova, D.H. Daurenbekov, K.B. Zhangylysov, Recombination luminescence in caso4, Radiat. Meas. 125 (2019) 19–24, http://dx.doi.org/10.1016/j.radmeas.2019.04.010, published June 2019.

[49] D.O. Junot, A.G. Santos, P.L. Antonio, M.V. Rezende, D.N. Souza, L.V. Caldas, Dosimetric and optical properties of caso4:tm and caso4:tm, ag crystals produced by a slow evaporation route, J. Lumin. 210 (2019) 58–65, http://dx.doi.org/10.1016/j.jlumin.2019.02.005.

[50] N.T. Mandlik, S.R. Rondiya, N.Y. Dzade, M. Kulkarni, P. Sahare, B. Bhatt, S. Dhole, Thermoluminescence, photoluminescence and optically stimulated luminescence characteristics of caso4:eu phosphor: Experimental and density functional theory (dft) investigations, J. Lumin. 221 (2020) 117051, http://dx.doi.org/10.1016/j.jlumin.2020.117051.

[51] A. Rodrigues, W. Santos, J. Rodrigues, E. Novais, G. Oliveira, A. Novais, D. Souza, Revealing the intrinsic nature of eu–doped lead phosphate: A study using density functional theory, Phys. B 666 (2023) 415104, http://dx.doi.org/10.1016/j.physb.2023.415104.

[52] B. Wu, A. Kumar, Extreme ultraviolet lithography: A review, J. Vac. Sci. Technol. B: Microelectron. Nanometer Struct. Process. Meas. Phenom. 25 (6) (2007) 1743–1761, http://dx.doi.org/10.1116/1.2794048.

[53] L. Yang, X. Zhou, X. Ni, L. Huang, L. Zeng, Z. Wang, J. Song, T. Fan, Quantitative prediction of optical static refractive index in complex oxides, Npj Comput. Mater. 11 (1) (2025) 162, http://dx.doi.org/10.1038/s41524-025-01539-9.

[54] R. Yang, Y. Ma, Q. Wei, D. Zhang, Properties of $cmc2_1$-x_2as_2o (x = si, ge, and sn) by first-principles calculations, Z. Nat.forsch. A 73 (11) (2018) 1025–1035, http://dx.doi.org/10.1515/zna-2018-0151.

[55] R. Huang, Z. Zheng, C. Gao, T. Zhang, M. Zhang, S. Li, H. Huang, K. Qiu, Effect of crystal-water on the optical and dielectric characteristics of calcium sulfate in the thz band, Opt. Express 32 (8) (2024) 13552–13561, http://dx.doi.org/10.1364/OE.520877.

[56] W. Han, K. Li, J. Dai, Y. Li, X. Li, Structural, mechanical, and thermodynamic properties of newly-designed superhard carbon materials in different crystal structures: a first-principles calculation, Comput. Mater. Sci. 171 (2020) 109229, http://dx.doi.org/10.1016/j.commatsci.2019.109229.

[57] H. yan Cheng, X. xin Zhang, G. liang Yu, T. min Cheng, Pressure-induced anomalous properties of laves phase and orthorhombic phase of yfe2, Phys. B 705 (2025) 417088, http://dx.doi.org/10.1016/j.physb.2025.417088.

[58] A. Reshak, M. Jamal, Dft calculation for elastic constants of orthorhombic structure within wien2k code: a new package (ortho-elastic), J. Alloys Compd. 543 (2012) 147–151, http://dx.doi.org/10.1016/j.jallcom.2012.07.107.

[59] G.L. Yu, T.M. Cheng, X.X. Zhang, Prediction of new stable phases of $fepd_2$ crystal alloy, J. Solid State Chem. 313 (2022) 123328, http://dx.doi.org/10.1016/j.jssc.2022.123328.

[60] W. Santos, A.M. Rodrigues, E. Novais, N. Frazão, A. Novais, D. Souza, Dft and dfpt calculations of the structural, electronic, optical, vibrational and thermodynamic properties of silicon tetraborate, Comput. Condens. Matter 35 (2023) e00796, http://dx.doi.org/10.1016/j.cocom.2023.e00796.

[61] D. Connétable, O. Thomas, First-principles study of the structural, electronic, vibrational, and elastic properties of orthorhombic NiSi, Phys. Rev. B 79 (9) (2009) 094101, http://dx.doi.org/10.1103/PhysRevB.79.094101.

[62] R.B. Tokas, S. Jena, P. Sarkar, S.R. Polaki, S. Thakur, S. Basu, N.K. Sahoo, Oblique angle deposition of hfo_2 thin films: Investigation of elastic and micro structural properties, 2014, http://dx.doi.org/10.48550/arXiv.1406.6858, arXiv preprint arXiv:1406.6858 [cond-mat.mtrl-sci], arXiv:1406.6858.

[63] K.C. Pitike, A.E. Marquez-Rossy, A. Flores-Betancourt, D.X. Chen, K. Santosh, V.R. Cooper, E. Lara-Curzio, On the elastic anisotropy of the entropy-stabilized oxide (mg, co, ni, cu, zn)o compound, J. Appl. Phys. 128 (1) (2020) 015101, http://dx.doi.org/10.1063/5.0011352.

[64] S. Pugh, Xcii. relations between the elastic moduli and the plastic properties of polycrystalline pure metals, Phil. Mag. 45 (367) (1954) 823–843, http://dx.doi.org/10.1080/14786440808520496.

[65] I.C. Stretton, P.F. Schofield, S. Hull, K.S. Knight, The static compressibility of gypsum, Geophys. Res. Lett. 24 (10) (1997) 1267–1270, http://dx.doi.org/10.1029/97GL01066.

[66] L. Giacomazzi, S. Scandolo, Gypsum under pressure: A first-principles study, Phys. Rev. B 81 (2010) 064103, http://dx.doi.org/10.1103/PhysRevB.81.064103.

[67] X. Zeng, S. You, L. Li, Z. Lai, G. Hu, W. Zhang, Y. Xie, Research on mechanical properties of high-pressure anhydrite based on first principles, Crystals 10 (4) (2020) http://dx.doi.org/10.3390/cryst10040240, https://www.mdpi.com/2073-4352/10/4/240.

[68] Z. Guan, H. Zhang, Y. Gao, P. Song, Y. Li, L. Wu, Y. Wang, Experimental–computational investigation of the elastic modulus of mortar under sulfate attack, Materials 16 (18) (2023) http://dx.doi.org/10.3390/ma16186167.